Advanced Li_2S/Si full battery enabled by TiN polysulfide immobilizer

Zhangxiang Hao,‡[a] Jie Chen,‡[a] Lixia Yuan,*[a] Qiming Bing,[b] Jingyao Liu,[b] Weilun Chen,[a] Zhen Li,[a] Feng Ryan Wang,[c] Yunhui Huang*[a]

[a] State Key Laboratory of Materials Processing and Die & Mould Technology, School of Materials Science and Engineering, Huazhong University of Science and Technology, Wuhan, Hubei 430074, China

[b] Laboratory of Theoretical and Computational Chemistry, Institute of Theoretical Chemistry, Jilin University, Changchun, Jilin 130023, China

[c] Department of Chemical Engineering, University College London, London WC1E 7JE, United Kingdom

E-mail: yuanlixia@hust.edu.cn (L. X. Yuan), huangyh@hust.edu.cn (Y. H. Huang).

‡ These authors contributed equally to this work.

Keywords: Li_2S/Si full battery, TiN polysulfide immobilizer, DFT calculations, lithium-sulfur battery

Abstract

Lithium sulfide (Li_2S) is a promising cathode material with high capacity, which can be paired with non-lithium metal anodes such as silicon or tin so that the safety issues caused by the Li anode can be effectively avoided. However, the Li_2S full cell suffers from rapid capacity degradation due to the dissolution of intermediate polysulfides. Here, we design a Li_2S/Si full cell with a Li_2S cathode incorporated by TiN polysulfide immobilizer within parallel hollow carbon (PHC). This full cell delivers a high initial reversible capacity of 702

mAh g_{Li2S}^{-1} (1007 mAh g_{sulfur}^{-1}) at 0.5 C rate and excellent cyclability with only 0.4% capacity fade per cycle over 200 cycles. The long cycle stability is ascribed to the strong polysulfide anchor effect of TiN and highly efficient electron/ion transport within the interconnected web-like architecture of PHC. Theoretical calculations, self-discharge measurements and anode stability experiments further confirm the strong adsorption of polysulfides on the TiN surface. The present work demonstrates that the flexible Li_2S cathode and paired Si anode can be used to achieve highly efficient Li-S full cells.

1. Introduction

There is a huge demand for new rechargeable systems with high energy densities, especially since the current lithium-ion batteries have approached their limit of theoretical energy density. [1-4] Lithium-sulfur (Li-S) batteries are believed to be the most promising candidates for next-generation electrochemical devices due to the super high specific theoretical capacity. [5-8] However, in practical application, Li-S batteries suffer from low sulfur utilization and severe shuttle effects, caused by low electronic conductivity of the sulfur species (S_8/Li_2S_2/Li_2S) and the dissolution of intermediate polysulfides (Li_2S_x, $3 \leq x \leq 8$) during the cathode process. Tremendous efforts have been made to enhance the electrochemical stability of the sulfur cathode and the shuttle phenomenon has been effectively overcome. Various nano-architecture sulfur composites[9-15] and/or novel polysulfides immobilizers[16-19] have been used to anchor the sulfur species within the cathode, alongside functional interlayers[20-22] to limit the migration of Li_2S_x within the cathode and optimized electrolyte components to control solubility of Li_2S_x. [23, 24] As a result, the

rechargeability of the sulfur cathode has significantly improved. With this problem being resolved, the safety issue at the Li metal anode becomes a bottleneck for Li-S battery viability. For a long time, the Li anode has suffered from Li dendrite growth, low Coulombic efficiency and safety issues. These problems make Li-S systems more complicated than other batteries with Li at the anode. The concentration and distribution of the dissolved Li_2S_x species within the electrolyte changes with the charge/discharge state, and hence the electrolyte around the Li anode changes throughout the cycle. This makes the formation and evolution of the solid electrolyte interface (SEI) highly complex, as a stable interface is difficult to achieve.

From this perspective, a cathode based on lithium sulfide (Li_2S) has unique advantages. The fully lithiated state of sulfur, Li_2S, can pair with a Li-free electrode such as silicon (Si) or tin (Sn), allowing the battery to address the safety issue of a Li anode. [25, 26] In addition, Li_2S shrinks during the initial charge process to form interspaces which reduce the volume change during the lithiation (discharge) process. Thus, the mechanical destruction of the cathode can be avoided, leading to improved cycle life. However, similar to sulfur cathodes, Li_2S cathodes inevitably encounter the "shuttle effect", leading to low Coulombic efficiency and a shortened cycle life. Meanwhile, Li_2S cathodes also suffer from low electronic and ionic conductivity of solid Li_2S and S_8, leading to low sulfur availability and poor rate performance. [27] For the Li_2S cathode, the strategies to enhance the electrochemical performance are similar to those used on the S_8 cathode, including decreasing the size of the Li_2S particles,[28-30] encapsulating Li_2S within a carbon host,[31-35] and employing transition metal disulfides to immobilize the Li_2S_x. [36,37] Such strategies have greatly improved the half-cell performances of Li-S batteries. However, the unavoidable shuttle effect still affects the fabrication of stable full cells with

Li_2S cathodes and non-Li anodes. [38] Herein, a high-performance Li_2S cathode with titanium nitride (TiN) incorporated into a parallel hollow carbon (PHC) host has been designed, which has successfully been used to construct a full cell with an Si anode. In this system, the hollow structure of PHC provides highly efficient electron and ion transport, while TiN works as a strong immobilizer for the dissolved Li_2S_x species. [39, 40] As a result, the Li_2S/Si full cell achieves a high reversible specific capacity of 702 mAh g_{Li2S}^{-1} (1007mAh g_{sulfur}^{-1}) at a rate of 0.5 C, with an excellent cycle life of only 0.4% capacity degradation per cycle over 200 cycles.

2. Results and discussion

Figure 1a illustrates the synthesis process of TiN/PHC@Li_2S. First, a precursor solution containing TiN, polyacrylonitrile (PAN), polymethyl methacrylate (PMMA) and N, N-dimethylformamide (DMF) was used to fabricate a nanofiber web through electrospinning. PMMA was pyrolysed by carbonization at 700 °C in a nitrogen atmosphere which generated parallel channels across the carbonized PAN. At the same time, TiN was uniformly dispersed in the hollow carbon host. Next, Li_2S was introduced into the channels of the TiN/PHC matrix using a simple slurry method. After being completely dried, binder-free flexible TiN/PHC@Li_2S cathodes were obtained which directly served as working electrodes for the measurements. PHC supported TiN nanoparticles efficiently adsorb Li_2S_x during the charge/discharge process (Figure 1b).

From Figure S1 (Supporting Information), we can see that the TiN/PHC precursor fibers have a smooth surface. The diameter of the fiber is ~800 nm and it is dozens of micrometers long. After carbonization, the surface of the TiN/PHC fibers becomes rough but the diameter

and length remain the same (**Figure 2**a and 2b). The surface roughness is attributed to the formation of TiN particles, as pure PHC fibers have a smooth surface after carbonization (Figure S2, Supporting Information). Scanning electron microscopy (SEM) images in Figure 2c and 2d reveal that when PMMA is added to the PAN precursor, a uniform microemulsion forms, which is stretched into nanoscale wires within the PAN fibers during the electrospinning process. With the following high-temperature pyrolysis, PMMA is decomposed to form nanochannels (Figure 2c). The cross-linked TiN/PHC fibers construct a flexible and free-standing matrix (Figure S3, Supporting Information). The mechanical flexibility of the TiN/PHC host was investigated by analyzing the dependence of electrical resistance on bending radius and bending angle (Figure S4, Supporting Information). It can be seen that the electrical resistance change of TiN/PHC increases dramatically when the bending radius reaches 18 mm, indicating that the TiN/PHC host may crack and cannot function as an electrode matrix when the bending radius is less than 18 mm, corresponding to a bending angle of more than 127°. Moreover, the electrical resistance change is nearly zero when the bending radius is above 18 mm and bending angle is less than 127°, revealing a good stability of electrical conductivity in this mechanical flexibility range. Loaded via a dip-coating process, the Li_2S nanoparticles were dispersed on the TiN/PHC nanofibers, to form the TiN/PHC@Li_2S electrode (Figure 2e). The X-ray diffraction (XRD) pattern of the TiN/PHC cathode shows four main diffraction peaks, which can be indexed to (111), (200), (220) and (311) reflections. This is in good agreement with the cubic phase of TiN (Fm3m, PDF#87-0632) as seen in the TiN/PHC matrix paper (Figure 2f). Additional diffraction peaks at 27°, 44° and 53° are observed for the TiN/PHC@Li_2S cathode, which can be assigned to

cubic Li_2S (Fm3m, PDF#65-2981). The XRD results demonstrate the successful fabrication of a flexible free-standing TiN/PHC@Li_2S cathode. To test the mass ratio of TiN to PHC in the host, we measured TG in oxygen atmosphere with a heating rate of 10 °C min^{-1} from 30 to 800 °C (Figure S5). After heating in oxygen, the TiN was turned to TiO_2 by maintaining the mass percent of 38% compared with the original TiN/PHC host. It can be calculated that the weight ratio of TiN to PHC is 29: 71 in the hybrid host. So in the whole cathode, the active Li_2S, TiN, PHC and super P are in a weight ratio of 45: 11: 26: 18. The content of Li_2S in the whole cathode is 45%.

Transmission electron microscopy (TEM) images clearly show the structure of the PHC fibers and the uniform parallel channels with a diameter of ~30 nm (**Figure 3**a-d). The abundant hollow regions of the nanofibers provide a large internal space for electrolyte infiltration. TiN nanoparticles with a diameter of ~30 nm were loaded both inside and outside the PHC fibers (Figure 3e and 3f). They effectively serve as Li_2S_x anchors to restrict the movement of intermediate products within the cathode during electrode reactions. [39, 40] A high-resolution TEM (HR-TEM) image reveals the polycrystalline structure of TiN with a well resolved lattice fringe of 0.24 nm, corresponding to the *d*-spacing of the (111) plane. TEM elemental mapping further confirms the distribution of TiN nanoparticles within the framework of the hollow N-doped carbon matrix (Figure 3f-i). The surface of TiN/PHC@Li_2S fibers become more rough due to the Li_2S coating (Figure S6a, b). From the TEM images and elemental mappings of N, Ti, S and C (Figure S6c-g), we can see that the area of sulfur is a little larger than those of Ti, N and C, indicating that the Li_2S is coated within the TiN/PHC matrix. The cathode volume is 11.1 mm^3 (Figure S7, Supporting

6

Information). The nitrogen sorption measurement shows that PHC has a porous structure with a specific surface area of only 11.1 m^2 g^{-1}, and the pore sizes are distributed between 7 and 100 nm (Figure S8a-b, Supporting Information). After TiN addition, the specific surface increases slightly (12.1 m^2 g^{-1}) and the pore size distribution maintains similar (Fig. S8c-d, Supporting Information). The small specific surface area should be ascribed to the large diameter of TiN/PHC fibers (~800 nm) and the large size of the parallel hollow pores (dozens of nanometer) (Figure 3).

To investigate the electrochemical performance, a cyclic voltammogram (CV) test was performed for the TiN/PHC@Li$_2$S cathode (**Figure 4**a). The cycle was first scanned to 3.6 V to overcome the barrier effect of the initial Li$_2$S cathode. The peak at 3.0 V, that appears only during the initial anode process, corresponds to the activation of inert Li$_2$S particles to form sulfur. This energy/voltage barrier can be reduced by charging at a low current and adding a Li$_2$S$_x$ additive during the charging process. The anodic peak located at 2.4 V in the following cycles is associated with the oxidation from Li$_2$S to Li$_2$S$_x$ and finally S$_8$. The cathodic peak of 2.3 V is attributed to the transition from S$_8$ to long-chain Li$_2$S$_x$ and the subsequent 2.0 V peak reflects the further reaction from Li$_2$S$_x$ to Li$_2$S$_2$/Li$_2$S. Figure 4b shows the charge/discharge profiles of the TiN/PHC@Li$_2$S cathode. The plateau during the initial charge is higher than those in the following charge curves because the micrometer Li$_2$S particles need to overcome the barrier with more energy, and the higher plateau of the initial charge process is one of the external manifestations for the barrier.[41] The following charge/discharge plateaus are similar to those of a typical Li-S cell. Two discharge voltage plateaus located at ~2.35 V and 2.10 V correspond to the standard two-step process during the discharge reaction, while the charge

voltage plateau at 2.37 V relates to the conversion of Li_2S to S. The discharge voltage plateau appears to drop in the following cycles when the current rate increases to 0.5 C. The rate performance of the $TiN/PHC@Li_2S$ cathode at various rates (ranging from 0.1 to 2 C) is shown in Figure 4c. The reversible discharge capacities are 829, 725, 619, 554, 505 and 465 mAh g_{Li2S}^{-1} (*i.e.*, 1190, 1040, 888, 795, 725 and 667 mAh g_{sulfur}^{-1}) at 0.1, 0.2, 0.5, 1, 1.5 and 2 C, respectively. When the rate is reset to 0.1 C after running at high current densities, a capacity of 698 mAh g_{Li2S}^{-1}(1002 mAh g_{sulfur}^{-1}) is recovered. This excellent rate performance is attributed to the high electronic conductivity of the $TiN/PHC@Li_2S$ cathode (0.39 mS cm^{-1}, Figure S9, Supporting Information) measured using the classic Hebb-Wagner method. The discharge/charge plateaus drop/rise when the current density increases, but two characteristic discharge plateaus integrally remain throughout the experiment (Figure 4d). Compared with the $TiN/PHC@Li_2S$ cathode in Figure 4c, $PHC@Li_2S$ exhibits a lower initial specific capacity of 721 mAh g_{Li2S}^{-1} (Figure S10 Supporting Information). Furthermore, for the $PHC@Li_2S$ cathode, the capacity gap between charge and discharge increases quickly in the initial 5 cycles, indicative of a lower Coulombic efficiency. The performance improvement in the $TiN/PHC@Li_2S$ cathode should be benefitted from the high electrical conductivity and polysulfide immobilization ability of TiN. Cycling at 0.2 C, the $TiN/PHC@Li_2S$ cathode achieves an initial capacity of 789 mAh g_{Li2S}^{-1} (1132 mAh g_{sulfur}^{-1}) and maintains 661 mAh g_{Li2S}^{-1} (949 mAh g_{sulfur}^{-1}) after 100 cycles (0.2 C) (Figure 4e). The mass ratio of Li_2S in the whole cathode is 45%. Therefore, the gravimetric capacity of the cathode is 355 mAh g^{-1} (0.2 C).

The anchoring effect of TiN and PHC was further investigated by comparing the self-discharge behaviors of PHC@Li$_2$S electrodes with and without TiN (**Figure 5**a and 5b). Both cells were run at 0.2 C for 8 cycles, then held at 2.1 V in the 9th discharge state for 3 days before resuming discharging procedure. It is clear that the discharge capacity of the cell without TiN is 868 mAh g$_{Li2S}^{-1}$ in the 8th cycle (abbreviated as C^{8th}) which decreases to a value of 803mAh g$_{Li2S}^{-1}$ after being held for 3 days (abbreviated as C^{9th}). In comparison, for the cell with TiN, C^{8th} is 857 mAh g$_{Li2S}^{-1}$ which drops to a C^{9th} value of 815 mAh g$_{Li2S}^{-1}$. For quantitative calculations, the self-discharge rate of the battery can be estimated by (C^{8th}–C^{9th})/C^{8th}×100%. With the incorporation of TiN, the self-discharge rate of the battery decreases from 7.5% to 4.9%, suggesting that TiN plays a significant role in restricting the diffusion of Li$_2$S$_x$. Figure 5c-e shows SEM images of the fresh Li anode and cycled Li anode disassembled from batteries with both PHC@Li$_2$S and TiN/PHC@Li$_2$S as cathodes. Compared to the fresh Li anode (Figure 5c), the cycled Li anode coupled with a PHC@Li$_2$S cathode (without TiN) (Figure 5d) shows a rough surface due to the high number of aggregated particles, forming Li dendrimers. This explains the high degree of corrosion of the Li anode during the charge/discharge cycle. In contrast, the cycled Li anode coupled with a TiN/PHC@Li$_2$S cathode reveals a dense and smooth surface (Figure 5e). A possible explanation is that the Li$_2$S$_x$ species are adsorbed by TiN. To further confirm the effect of TiN on Li anode safety, we assembled two coin cells using cycled Li anodes (with and without TiN) as the working electrodes and fresh Li foil as the counter electrode. Figure 5f shows the charge/discharge voltage profiles of these Li/Li batteries at a current density of 0.44 mA cm^{-2}. Clearly, the cell with a cycled Li anode from the TiN-containing battery exhibits much lower

and more stable overpotential for 350 h, which confirms that a Li anode paired with a TiN/PHC@Li$_2$S cathode can form a more stable SEI and suppress electrolyte consumption. On the contrary, the cycled Li foil paired with a PHC@Li$_2$S cathode without TiN has an uneven surface which cannot prevent side reactions between Li metal and the electrolyte effectively.

To further understand the anchoring mechanism of TiN which confines the dissolved Li$_2$S$_x$, the adsorption of Li$_2$S$_4$, Li$_2$S$_6$ and Li$_2$S$_8$ on the TiN (200) surface, confirmed to be the major crystal plane by XRD, was studied using density functional theory (DFT) calculations. The optimized adsorption structures and isosurfaces of the charge density difference for Li$_2$S$_4$, Li$_2$S$_6$ and Li$_2$S$_8$ are shown in **Figure 6** and S11 (Supporting Information). The adsorption energy (E_{ads}) of Li$_2$S$_x$ ($x = 4, 6, 8$) on TiN (200) is calculated as:

$E_{ads} = E_{total} - (E_{sur} + E_{mol})$

where E_{total} is the total energy of the adsorption system, E_{sur} is the total energy of the TiN (200) surface, and E_{mol} is the total energy of the Li$_2$S$_x$ molecule. Based on this equation, a more negative E_{ads} indicates a stronger adsorption capability. The effective charge (Q_X) was calculated using Henkelkman's grid-based algorithm with the Bader electron decomposition method which gives the equation: $Q_X = Z_X - q_{Bader,X}$, where Z_X is the number of valence electrons in X atom and $q_{Bader,X}$ is the calculated Bader charge. Based on the calculation, the Bader charge analysis of TiN (200) suggests that the surface Ti atom has a positive charge of +0.45 |e| and the surface N atom has a negative charge of -0.44 |e|, which can both separately act as adsorption sites for S$_x^{2-}$ and Li$^+$ ions. The calculated adsorption systems of Li$_2$S$_x$ on TiN (200), Li$_2$S$_4$, Li$_2$S$_6$ and Li$_2$S$_8$ possess high adsorption energies of -4.41, -4.35 and -4.40 eV

(Table S1, Supporting Information), respectively. The optimized adsorption structures with charge density difference (CDD) plots for different Li_2S_x adsorbates are shown in Figure 6. With the growth of the sulfur chain in Li_2S_x, the Ti-S bond length decreases from 2.71 to 2.64 Å (Table S1) while the negative charge on the terminal sulfur atoms in the sulfur chain change from -0.63 to -0.69 |e| (**Table 1**). The CDD plots clearly show the electron transfer and the formation of electrovalent bonds between the Li_2S_x adsorbates and the TiN (200) surface. These results suggest that the TiN (200) surface has a strong adsorption to Li_2S_x molecules via chemical interaction, which is consistent with the experimental result in which TiN powder has a strong adsorption capacity for Li_2S_x in Li-S batteries.[20] The experiment visualized in Figure S12 (Supporting Information) offers straightforward evidence of the strong sorption ability of TiN particles. In the case of PHC host (N-doped carbon from a PAN precursor), the adsorption is not evident between PHC host and polysulfides. In addition, CV curves were examined within a voltage range of -0.8 to 0.8 V for symmetrical Li_2S_6 batteries (Figure S13, Supporting Information). The polarization curves reveal major fraction of redox current of Li_2S_6. The current density increases with the addition of TiN, suggesting that the TiN-polysulfide interaction not only statically exists but dynamically accelerates the electrochemical reactions of Li_2S_x.

The TiN/PHC@Li_2S cathode clearly exhibits high adsorption of Li_2S_x and good cycling stability. At 0.5 C, the TiN/PHC@Li_2S cathode achieves an initial capacity of 700 mAh g_{Li2S}^{-1} (1004 mAh g_{sulfur}^{-1}) and maintains 504 mAh g_{Li2S}^{-1} (723mAh g_{sulfur}^{-1}) after 400 cycles, corresponding to a capacity fade of only 0.08% per cycle (**Figure 7**a). With a mass loading of 3.4 mg_{Li2S} cm^{-2}, this TiN/PHC@Li_2S cathode has excellent cycle stability and capacity

retention, higher than the values recorded for the PHC@Li$_2$S cathode (without TiN) in a half cell. With increasing the current density to 1 C, the TiN/PHC@Li$_2$S cathode achieves an initial reversible capacity of 835 mAh g$_{sulfur}^{-1}$ and maintains 483 mAh g$_{sulfur}^{-1}$ after 600 cycles, corresponding to a capacity fade of only 0.09% per cycle. In contrast, the reversible capacity of PHC@Li$_2$S cathode decreases quickly after 150 cycles and maintains only about 100 mAh g$_{sulfur}^{-1}$ after 600 cycles (Figure S14, Supporting Information). This superior performance gives the "TiN/PHC@Li$_2$S|Si" full cell a high reversible specific capacity of 702 mAh g$_{Li2S}^{-1}$ (1007 mAh g$_{sulfur}^{-1}$) at 0.5 C (Figure 7b), comparable to a Li$_2$S/Li half cell. The full cell shows good rate performance (Figure S15, Supporting Information). Moreover, it displays slightly lower charge/discharge plateaus than those in the Li$_2$S/Li half cell due to the utilization of the Si anode (Figure S16, Supporting Information). Profiting from the excellent Li$_2$S$_x$ immobilization effect of the PHC/TiN hybrid host, the "TiN/PHC@Li$_2$S|Si" full cell demonstrates a cyclability with only 0.4% capacity fade per cycle over 200 cycles, better than the "PHC@Li$_2$S|Si" full cell. The structure of the Si electrode before and after cycling at 0.5 C was observed by SEM images (Figure S17). The particle size of the fresh Si is several micrometers. The conductive agent (super P) and the binder molecules are distributed around the Si particles (Figure S17a-c). Elemental mappings of C, Si and S reveal that C and Si particles disperse in the whole electrode, but S is absent in the anode (Figure S17d-f). After 50 cycles, the Si electrode shows a morphology similar to the fresh electrode, except the particle size becomes larger due to the residual volume effect or the residual lithiated-Si (Figure S17g-k). Moreover, the signal of S element appears in Figure S17 l, indicating that some polysulfide has diffused from Li$_2$S cathode to Si anode (shuttle effect). The Si-Li$_2$S full

cell shows faster capacity loss than that of the half cells (Figure 7). For the half cells, whether the Si half cell or the Li_2S half cell, the counter electrodes are lithium foil which can provide Li mass exceeding the theoretical amount by more than 100 times. So the Coulombic efficiency of the half cells was tested at the condition that the counter lithium electrode can offer enough lithium ions during the whole discharge process. The N/P ratio (capacity) in the Si-Li_2S full cell is only 1.2-1.3. Both the Li_2S cathode and Si anode contribute to the capacity loss. This is also the reason that the full cell shows lower Coulombic efficiency than that of the half cell. We choose the Li_2S electrode with 3.4 mg cm^{-2} loading to calculate the gravimetric energy density of the cell. The cell parameters for energy density estimation (including all components except cell-housing) are provided in **Table S2**. With specific capacity of 702 mAh g^{-1} and Li_2S loading of 3.4 mg cm^{-2}, the estimated gravimetric energy density of the $TiN/PHC@Li_2S|Si$ full cell is ~252 Wh kg^{-1}.

3. Conclusions

In summary, a Li_2S/Si full cell was successfully constructed, featuring a novel $TiN/PHC@Li_2S$ cathode. In this rational design, the PHC matrix served as a conductive network to maximize sulfur utilization and improve the mechanical properties of the free-standing cathode. TiN nanoparticles were found to immobilize dissolved Li_2S_x intermediates effectively and suppress the shuttle effect. The highly conductive TiN also enhanced the electronic conductivity of the cathode. The corresponding Li_2S/Si full cell demonstrates a high reversible capacity of 702 mAh g_{Li2S}^{-1} (1007 mAh g_{sulfur}^{-1}) at 0.5 C and good cycle stability with only 0.4% capacity degradation per cycle. These results show that

the integrated electrode design holds great promise in the development of high-performance Li$_2$S cathodes for next-generation rechargeable batteries with high energy density using non-lithium metal anodes.

4. Experimental sections

Synthesis of TiN/PHC@Li$_2$S cathode:

A precursor solution was prepared by dissolving 0.3 g TiN, 0.3 g PMMA and 1.5 g PAN in 15 ml DMF under ultrasonic stirring for 1 h followed by overnight stirring at 80 °C. The solution was electrospun on a collector to achieve PAN/PMMA/TiN composite nanofibers. The distance between the syringe and the collector was fixed at 15 cm, and the voltage was set at 17 kV with a flow rate of 0.8 ml h^{-1}. The electrospun fibers were kept at 80 °C for 6 h, calcined in nitrogen at 250 °C for 3 h and then at 700 °C for another 2 h with 3 °C min^{-1} ramp rate. The flexible TiN/PHC paper obtained was punched into discs.

Li$_2$S and N-methylpyrrolidone (NMP, 99%) were purchased from Sigma-Aldrich. Homogeneous Li$_2$S slurry was fabricated by mixing 70 mg Li$_2$S and 30 mg super P in 1 ml NMP under vigorous stirring overnight. The as-prepared flexible TiN/PHC paper was immersed in the slurry for 15 seconds, and then removed and placed in a vacuum oven at 80 °C overnight to obtain the TiN/PHC@Li$_2$S cathode. The diameter of the cathode was 8 mm and the resulting active material (Li$_2$S) loading was 2.5–3.5 mg cm^{-2}. The PHC@Li$_2$S cathode was fabricated using the same method but without the addition of TiN during the electrospinning process.

Preparation of Si anode and activation:

Si powder (Haotian Nano Tech. Comp., China) was ball-milled for 2 h in water. After vacuum seasoning, the product was heated at 1000 °C for 2 h. The heated Si was etched using 0.5 M hydrogen fluoride (HF) for 2 h to remove surface silicon dioxide (SiO_2). During the anode preparation, the above Si powder, super P, and polyacrylic acid (PAA) were dispersed in deionized water in a weight ratio of 70: 15: 15. The resulting slurry was coated onto copper foil and dried in a vacuum. Then the anode was roll pressed and punched to form round discs with mass loading to match with the cathode capacity. To avoid interference from the low initial Coulombic efficiency of Si, the Si anode was activated by charging/discharging for 3 cycles at 0.1 C from 0.01 to 1.5 V with a Si/Li half cell (stopped at discharge state). The disassembled Si electrode was used as the anode in the Li_2S/Si full cell. The diameter of the activated-Si anode was also 8 mm. The mass loading of the Si anode was 1.2-1.8 mg cm^{-2}, and the N/P ratio (capacity) was 1.2-1.3 in the full cell.

Characterization:

XRD patterns were obtained by the equipment (Holland, PANalytical X'pert PRO-DY2198) at 40 mA and 40 kV using Cu Kα radiation. The structure and morphology of TiN/PHC and TiN/PHC@Li_2S were collected using SEM (Sirion 200, FEI), and HR-TEM images of TiN/PHC@Li_2S samples were observed under Tecnai G200 in Holland. The Brunauer-Emmett-Teller (BET) surface area was calculated according to the adsorption data in the relative pressure range from 0.06 to 0.2. The mass ratio of TiN/PHC was determined by TG analysis (PerkinElmer) in oxygen atmosphere with a heating rate of 10 °C min^{-1} from 30 to 800 °C.

Electrochemical measurements:

All the electrochemical measurements were performed on 2032 coin cells. Celgard 2400 served as a separator. The electrolyte was 1 M lithium bis(trifluoromethylsulfonyl)imide(LiTFSI) in a well mixed solution of 1, 2-dimethoxyethane (DME) and 1,3-dioxolane (DOL) (1:1 v/v) with 2 wt.% lithium nitrate (LiNO$_3$) and 0.02 M Li$_2$S$_6$ as additives. Li$_2$S$_6$ solution was fabricated by adding a certain weight of S and Li$_2$S powder in the electrolyte and stirring overnight. The anode was Li foil for Li$_2$S/Li half cell, and an activated-Si electrode for the Li$_2$S/Si full cell. The ratio of sulfur to electrolyte was maintained at 1:10 for both Li$_2$S/Li half cell and Li$_2$S/Si full cell. The Li$_2$S$_6$ additive in electrolyte contributed ~3.8% to the total capacity. CV measurements were operated on a workstation (CHI614b) at 0.03 mV s^{-1} rate with a voltage range of 1.7–3.6 V versus Li$^+$/Li in the initial cycle and then a rate of 0.05 mV s^{-1} with a voltage range of 1.7–2.8 V in subsequent cycles. Galvanostatic charge/discharge was tested by a battery testing system (Neware, China) in a voltage window of 3.6–1.7 V at 0.05 C in the initial cycle, and then between 1.7 and 2.8 V for the Li$_2$S/Li half cell. For the Li$_2$S/Si full cell, the voltage window of galvanostatic charge/discharge was 1.3–3.8 V at 0.05 C in the initial cycle, then between 1.3 and 2.8 V during subsequent cycles. Electronic conductivity was measured by the Hebb-Wagner method as shown in detail in Figure S9 (Supporting Information).

Symmetrical cell assembly and measurement:

The evaluation method followed the previously reported procedure.[42] The electrodes for symmetrical batteries were free-standing TiN/PHC and PHC hosts in the absence of sulfur species. These free-standing hosts were used as identical counter and working electrodes, with

16

an electrolyte (30 μl) containing 1 mol l^{-1} LiTFSI, 0.2 M Li_2S_6 and 2 wt% $LiNO_3$ in DOL/DME (v/v=1/1). The same electrolyte without Li_2S_6 was used as a control sample. CV measurement of the symmetrical cells was performed from -0.8 to 0.8 V at 0.05 V s^{-1}.

Computational methods:

First-principles spin-polarized DFT calculations were performed using the Vienna ab initio Simulation Package (VASP).[43] The projector augmented wave (PAW) pseudopotential[44] was used to describe the interactions between electrons and ions. The Perdew-Burke-Ernzerhof exchange-correlation functional of the generalized-gradient approximation (PBE-GGA)[45] was adopted to describe the exchange–correlation energy. A plane-wave base, set with an energy cut-off of 400 eV, was applied to all calculations.

The optimized bulk geometry of TiN was calculated based on the experimental crystal structure [32]. The Brillouin zone was sampled using (7×7×7) Monkhorst-Pack special k-point for the optimization of bulk structure. The lattice constant and atomic position of the bulk was fully relaxed until the forces exerted on each atom converged to within 0.02 eVÅ^{-1}. The optimized bulk structure of TiN was in agreement with the experimental structure. A four-atom-thick surface slab model of the TiN (200) surface with a (3×3) supercell containing 144 atoms was constructed based on the optimized bulk structure of TiN. In the optimization of the TiN (200) surface, the Monkhorst-Pack k-point was sampled as (5×5×1) while the convergence criterion was the same as in the calculation of bulk structure. During the optimization, the upper two atomic layers of the slab model could fully relax while the bottom two layers were fixed at the optimized bulk geometry. A vacuum region of 15Å was inserted

between the periodic slabs along the perpendicular direction of the surface to avoid interlayer

interactions.

Supporting Information

Supporting Information is available online from the Wiley Online Library or from the author.

Received: ((will be filled in by the editorial staff))
Revised: ((will be filled in by the editorial staff))
Published online: ((will be filled in by the editorial staff))

References

[1] P. G. Bruce, S. A. Freunberger, L. J. Hardwick and J. M. Tarascon, *Nat. Mater.*, **2012**, *11*, 19.

[2] M. Wild, L. O'Neill, T. Zhang, R. Purkayastha, G. Minton, M. Marinescu and G. J. Offer, *Energy Environ. Sci.*, **2015**, *8*, 3477.

[3] Z. Li, Y. Huang, L. Yuan, Z. Hao and Y. Huang, *Carbon*, **2015**, *92*, 41.

[4] D. Su, D. Zhou, C. Wang and G. Wang, *Adv. Funct. Mater.*, **2018**, 1800154.

[5] Y.-J. Li, J.-M. Fan, M.-S. Zheng and Q.-F. Dong, *Energy Environ. Sci.*, **2016**, *9*, 1998.

[6] Q. Pang, X. Liang, C. Y. Kwok and L. F. Nazar, *Nature Energy*, **2016**, *1*, 16132.

[7] Y. Sun, N. Liu and Y. Cui, *Nature Energy*, **2016**, *1*, 16071.

[8] A. Manthiram, S. H. Chung and C. Zu, *Adv. Mater.*, **2015**, *27*, 1980.

[9] X. Li, J. Liang, K. Zhang, Z. Hou, W. Zhang, Y. Zhu and Y. Qian, *Energy Environ. Sci.*, **2015**, *8*, 3181.

[10] M. Li, R. Carter, A. Douglas, L. Oakes and C. L. Pint, *ACS Nano*, **2017**, *11*, 4877.

[11] G. Hu, Z. Sun, C. Shi, R. Fang, J. Chen, P. Hou, C. Liu, H.-M. Cheng and F. Li, *Adv. Mater.*, **2017**, *29*, 1603835.

[12] Z. Li, L. Yuan, Z. Yi, Y. Sun, Y. Liu, Y. Jiang, Y. Shen, Y. Xin, Z. Zhang and Y. Huang, *Adv. Energy Mater.*, **2014**, *4*, 1301473.

[13] X. Ji, K. T. Lee and L. F. Nazar, *Nat. Mater.*, **2009**, *8*, 500.

[14] W. Li, G. Zheng, Y. Yang, Z. W. Seh, N. Liu and Y. Cui, *PNAS*, **2013**, *110*, 7148.

[15] J. Yan, B. Li and X. Liu, *Nano Energy*, **2015**, *18*, 245.

[16] Z. Hao, R. Zeng, L. Yuan, Q. Bing, J. Liu, J. Xiang and Y. Huang, *Nano Energy*, **2017**, *40*, 360.

[17] J. Pu, Z. Shen, J. Zheng, W. Wu, C. Zhu, Q. Zhou, H. Zhang and F. Pan, *Nano Energy*, **2017**, *37*, 7.

[18] Z. Li, J. Zhang, B. Y. Guan and X. W. D. Lou, *Angew. Chem., Int. Ed.*, **2017**, *56*, 16003.

[19] Y. Song, W. Zhao, L. Kong, L. Zhang, X. Zhu, Y. Shao, F. Ding, Q. Zhang, J. Sun and Z. Liu, *Energy Environ. Sci.*, **2018**, *11*, 2620.

[20] S. H. Chung and A. Manthiram, *Adv. Mater.*, **2014**, *26*, 7352.

[21] Z. X. Hao, L. X. Yuan, Z. Li, J. Liu, J. W. Xiang, C. Wu, R. Zeng and Y. H. Huang, *Electrochim. Acta*, **2016**, *200*, 197.

[22] S. H. Chung, C. H. Chang and A. Manthiram, *ACS Nano*, **2016**, *10*, 10462.

[23] Z. Lin, Z. Liu, W. Fu, N. J. Dudney and C. Liang, *Adv. Funct. Mater.*, **2013**, *23*, 1064.

[24] E. Rangasamy, J. Li, G. Sahu, N. Dudney and C. Liang, *J. Am. Chem. Soc.*, **2014**, *136*, 6874.

[25] H. Jha, I. Buchberger, X. Cui, S. Meini and H. A. Gasteiger, *J. Electrochem. Soc.*, **2015**, *162*, A1829.

[26] C. Nan, Z. Lin, H. Liao, M. K. Song, Y. Li and E. J. Cairns, *J. Am. Chem. Soc.*, **2014**, *136*, 4659.

[27] F. Wu, J. T. Lee, F. Fan, N. Nitta, H. Kim, T. Zhu and G. Yushin, *Adv. Mater.*, **2015**, *27*, 5579.

[28] C. Wang, X. Wang, Y. Yang, A. Kushima, J. Chen, Y. Huang and J. Li, *Nano Lett.*, **2015**, *15*, 1796.

[29] Y. Yang, G. Zheng, S. Misra, J. Nelson, M. F. Toney and Y. Cui, *J. Am. Chem. Soc.*, **2012**, *134*, 15387.

[30] G. Tan, R. Xu, Z. Xing, Y. Yuan, J. Lu, J. Wen, C. Liu, L. Ma, C. Zhan, Q. Liu, T. Wu, Z. Jian, R. Shahbazian-Yassar, Y. Ren, D. J. Miller, L. A. Curtiss, X. Ji and K. Amine, *Nature Energy*, **2017**, *2*, 17090.

[31] Y. Fu, Y.-S. Su and A. Manthiram, *Adv. Energy Mater.*, **2014**, *4*, 1300655.

[32] L. Wang, Y. G. Wang and Y. Y. Xia, *Energy Environ. Sci.*, **2015**, *8*, 1551.

[33] H. J. Peng, J. Q. Huang, X. Y. Liu, X. B. Cheng, W. T. Xu, C. Z. Zhao, F. Wei and Q. Zhang, *J. Am. Chem. Soc.*, **2017**, *139*, 8458.

[34] K. Cai, M. K. Song, E. J. Cairns and Y. Zhang, *Nano Lett.*, **2012**, *12*, 6474.

[35] F. Han, J. Yue, X. Fan, T. Gao, C. Luo, Z. Ma, L. Suo and C. Wang, *Nano Lett.*, **2016**, *16*, 4521.

[36] Z. W. Seh, H. Wang, P.-C. Hsu, Q. Zhang, W. Li, G. Zheng, H. Yao and Y. Cui, *Energy Environ. Sci.*, **2014**, *7*, 672.

[37] G. Zhou, J. Sun, Y. Jin, W. Chen, C. Zu, R. Zhang, Y. Qiu, J. Zhao, D. Zhuo, Y. Liu, X. Tao, W. Liu, K. Yan, H. R. Lee and Y. Cui, *Adv. Mater.*, **2017**, *29*, 1603366.

[38] M. Liu, Y. X. Ren, H. R. Jiang, C. Luo, F. Y. Kang and T. S. Zhao, *Nano Energy*, **2017**, *40*, 240.

[39] Z. Cui, C. Zu, W. Zhou, A. Manthiram and J. B. Goodenough, *Adv. Mater.*, **2016**, *28*, 6926.

[40] Z. Hao, L. Yuan, C. Chen, J. Xiang, Y. Li, Z. Huang, P. Hu and Y. Huang, *J. Mater. Chem. A*, **2016**, *4*, 17711.

[41] Y. Yang, G. Zheng, S. Misra, J. Nelson, M. Toney and Y. Cui, *J. Am. Chem. Soc.*, **2012**, *134*, 15387.

.[42] Z. Yuan, H. J. Peng, T. Z. Hou, J. Q. Huang, C. M. Chen, D. W. Wang, X. B. Cheng, F. Wei and Q. Zhang, *Nano Lett.*, **2016**, *16*, 519.

[43] G. Kresse and J. Furthmüller, *Phys. Rev. B*, **1996**, *54*, 11169.

[44] P. E. Blöchl, *Phys. Rev. B*, **1994**, *50*, 17953.

[45] J. P. Perdew, K. Burke and M. Ernzerhof, *Phys. Rev. Lett.*, **1996**, *77*, 3865.
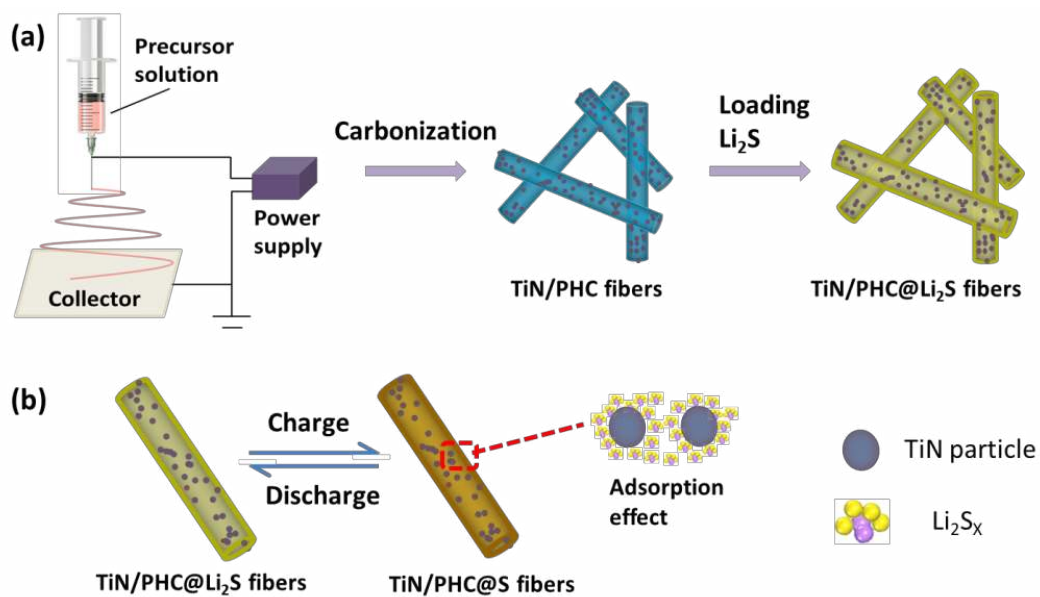
Figure 1 Schematic illustration of (a) the synthesis process of TiN/PHC@Li$_2$S fibers and (b) adsorption effect of TiN in charge/discharge process.
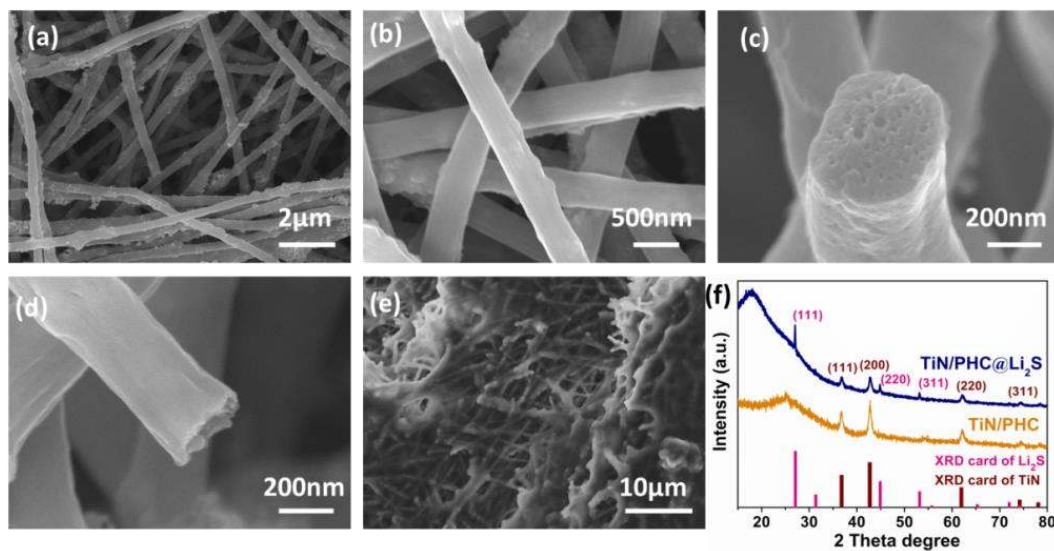
Figure 2 SEM image of (a, b) TiN/PHC fibers, (c, d) cross-link TiN/PHC fibers and (e) TiN/PHC@Li$_2$S fiber paper. (f) XRD patterns of TiN/PHC@Li$_2$S and TiN/PHC composite.
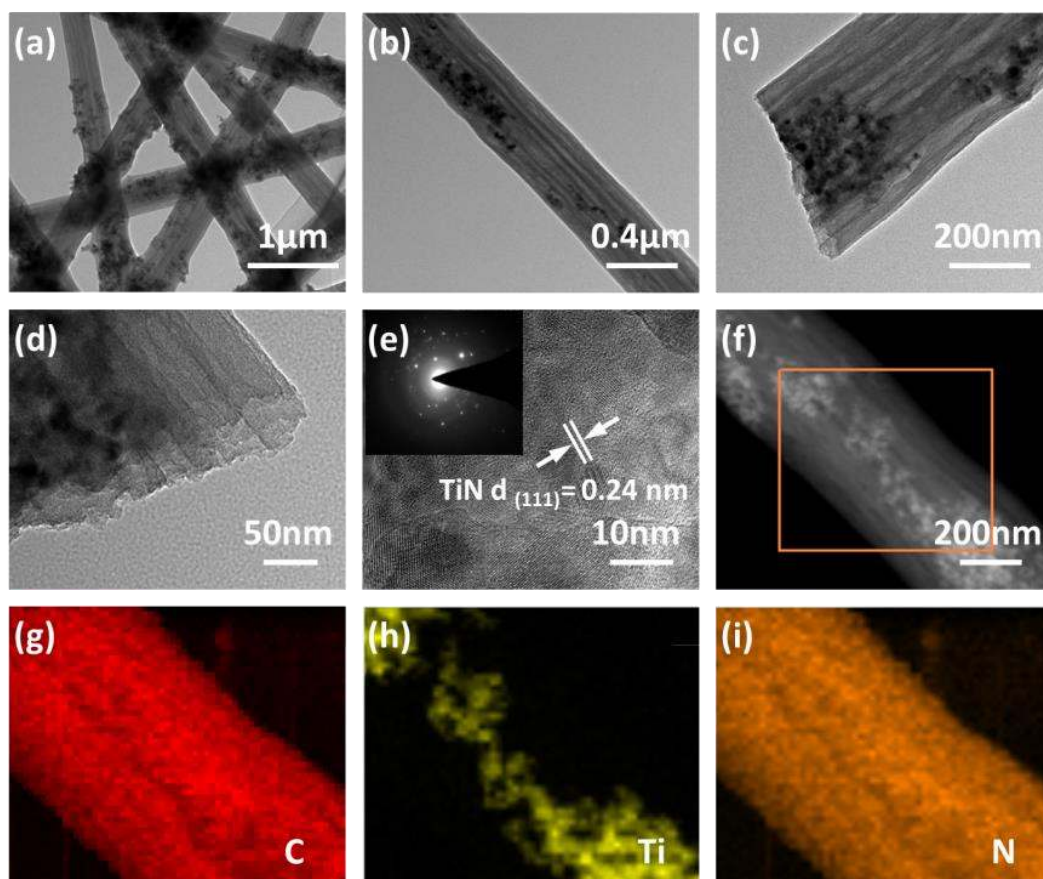
Figure 3 Characterizations of the TiN/PHC paper. (a-e) TEM images, (f) dark-field TEM image and corresponding element mappings of (g) carbon, (h) titanium and (i) nitrogen.
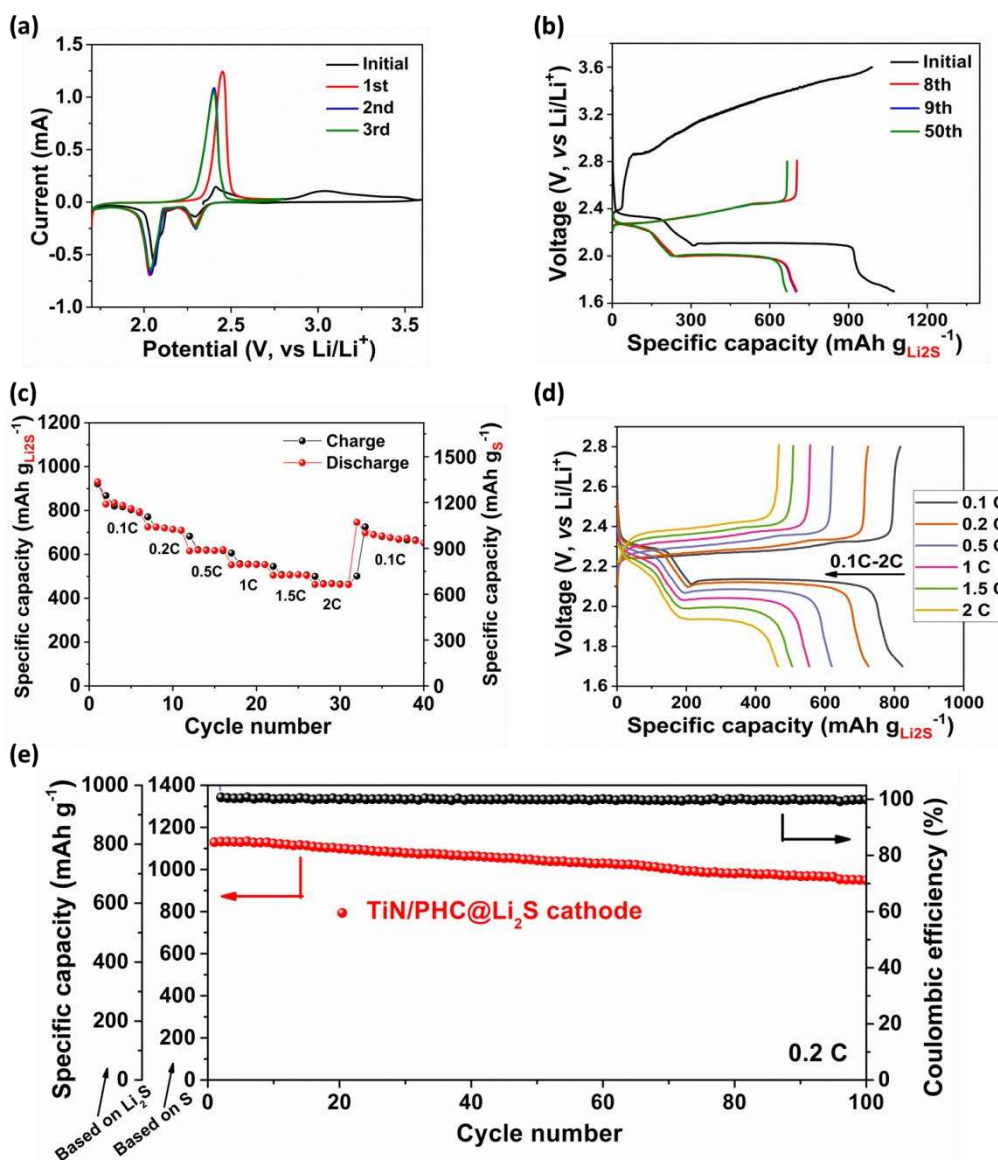
Figure 4(a) CV curves of the TiN/PHC@Li₂S cathode *vs.* Li for half-cell between 1.7 and 3.6 V at the initial cycle and the following 3 cycles scan from 1.7 to 2.8 V. (b) Charge and discharge profiles of TiN/PHC@Li₂S cathode *vs.* Li for half-cell at 0.05 C at initial cycle and at 0.5 C in 8th, 9th and 50th cycles. (c) Rate performance of the TiN/PHC@Li₂S cathode *vs.* Li for half-cell with a current rate ranging from 0.1 to 2 C rate. (d) Voltage *vs.* specific capacity profiles at various rates of TiN/PHC@Li₂S half-cell. (e) Cycling performance and corresponding Coulombic efficiency based on Li₂S/Li half-cell at 0.2 C for TiN/PHC@Li₂S cathode.
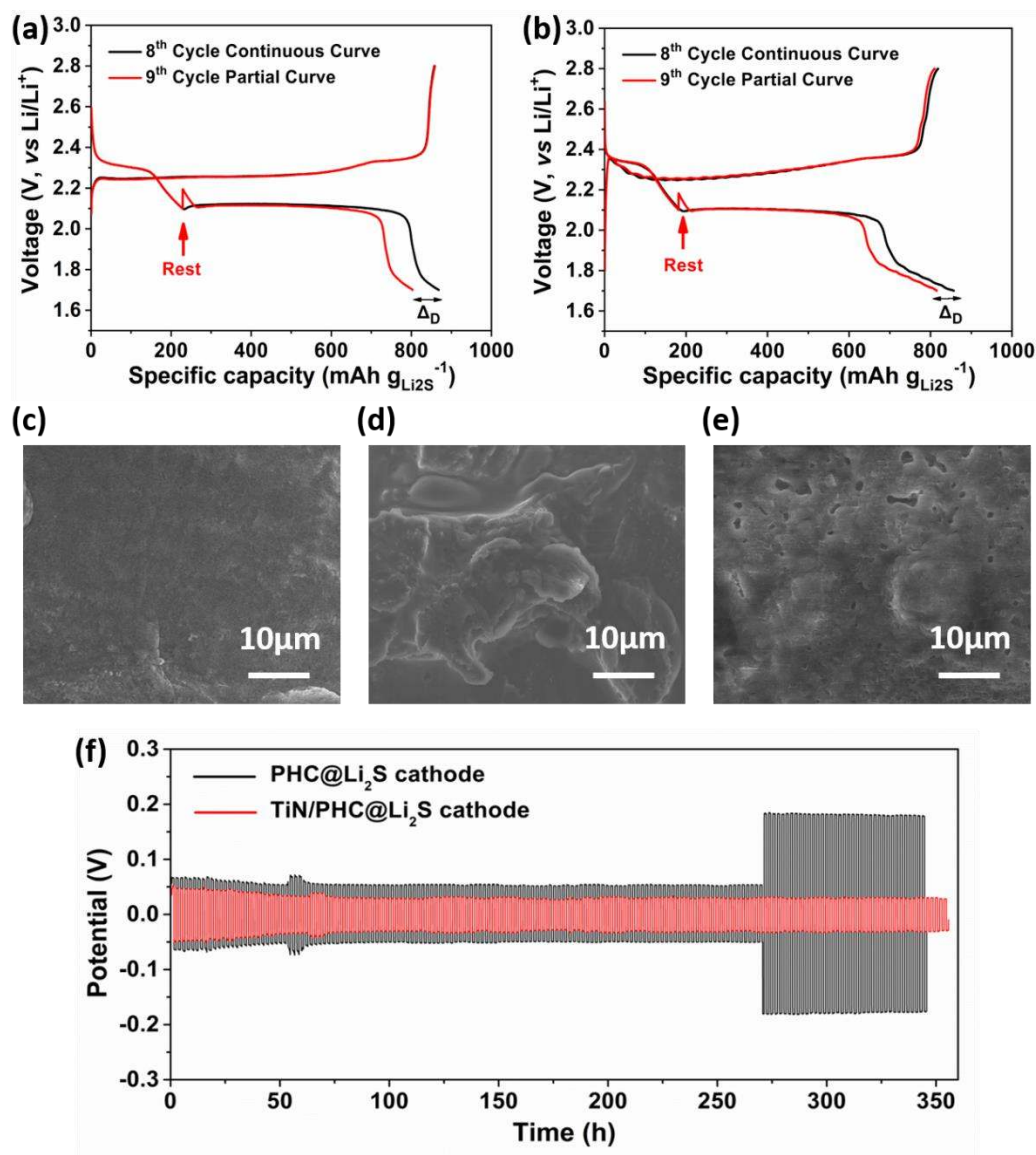
Figure 5 Self-discharge tests of (a) PHC@Li$_2$S electrode and (b) TiN/PHC@Li$_2$S electrode at

0.2 C rate. SEM images of (c) fresh Li anode, (d) cycled Li anode coupled with PHC@Li$_2$S

cathode and (e) cycled Li foil coupled with TiN/PHC@Li$_2$S electrode. (f) Time and potential

profiles of the Li/Li cells employing the cycled Li electrode coupled with the two composite

electrodes: the current density of the Li/Li cell was set at 0.44 mA cm^{-2} and lasted for 1 h per

half-cycle.
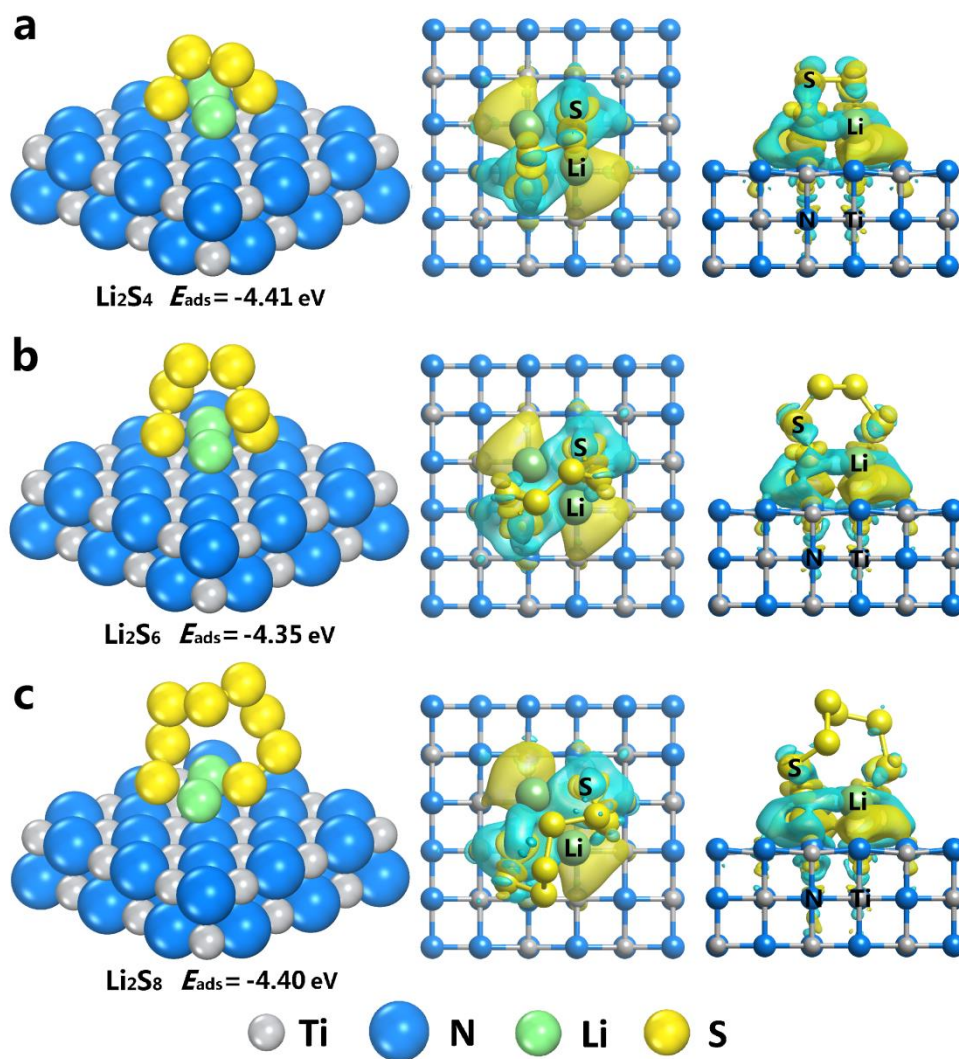
Figure 6 The adsorption structures, adsorption energies and the charge density difference plots for (a) Li_2S_4, (b) Li_2S_6 and (c) Li_2S_8 on TiN (200). Color scheme: gray, Ti; blue, N; green, Li; yellow, S. In the charge density difference plots, yellow surfaces correspond to charge gains and blue surfaces correspond to an equivalent charge lost.
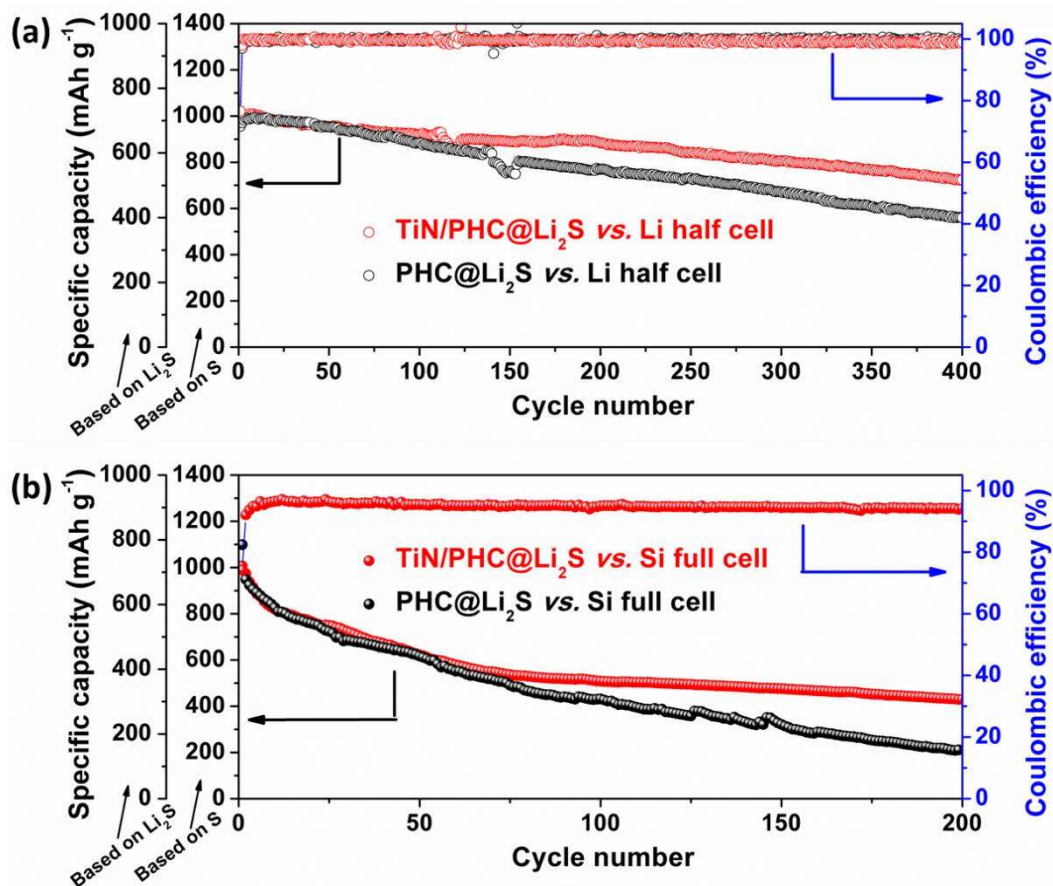
Figure 7 Cycling performance and Coulombic efficiency of TiN/PHC@Li$_2$S and PHC@Li$_2$S

cathode (a) *vs.* Li half cell at 0.5 C, (b) *vs.* Si full cell at 0.5 C.

Table 1. Calculated effective charges of Li and S atoms of Li_2S_4, Li_2S_6 and Li_2S_8 on TiN (200).

Adsorbate	Li	S
Li_2S_4	+0.86	-0.63
Li_2S_6	+0.86	-0.64
Li_2S_8	+0.86	-0.69

Supporting Information

Advanced Li$_2$S/Si full battery enabled by TiN polysulfide immobilizer

Zhangxiang Hao,‡[a] Jie Chen,‡[a] Lixia Yuan,[a] Qiming Bing,[b] Jingyao Liu,[b] Weilun Chen,[a]*

Zhen Li,[a] Feng Ryan Wang,[d] Yunhui Huang[ac]*
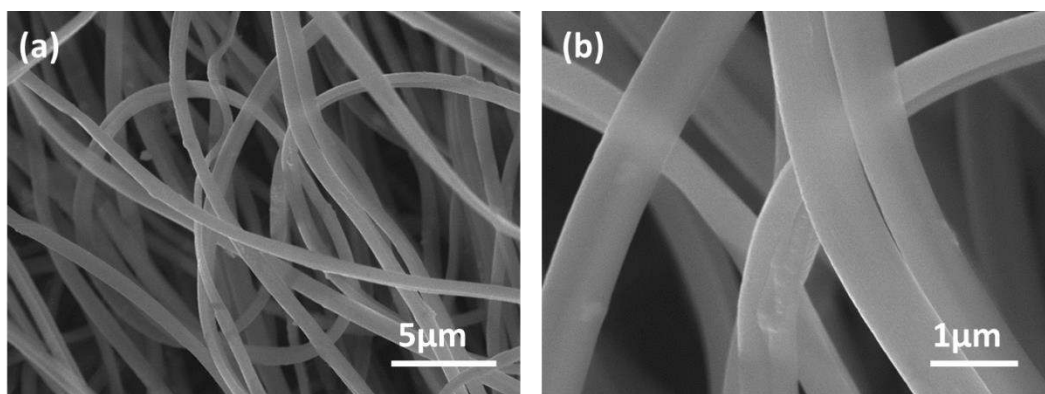
Figure S1 SEM images of (a) (b) TiN/PHC precursor by electrospinning.
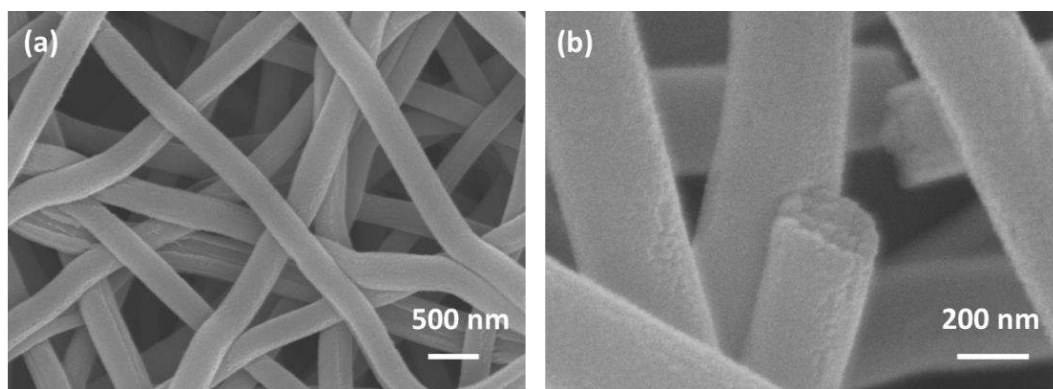
Figure S2 SEM images of (a) (b) PHC fibers (without TiN).
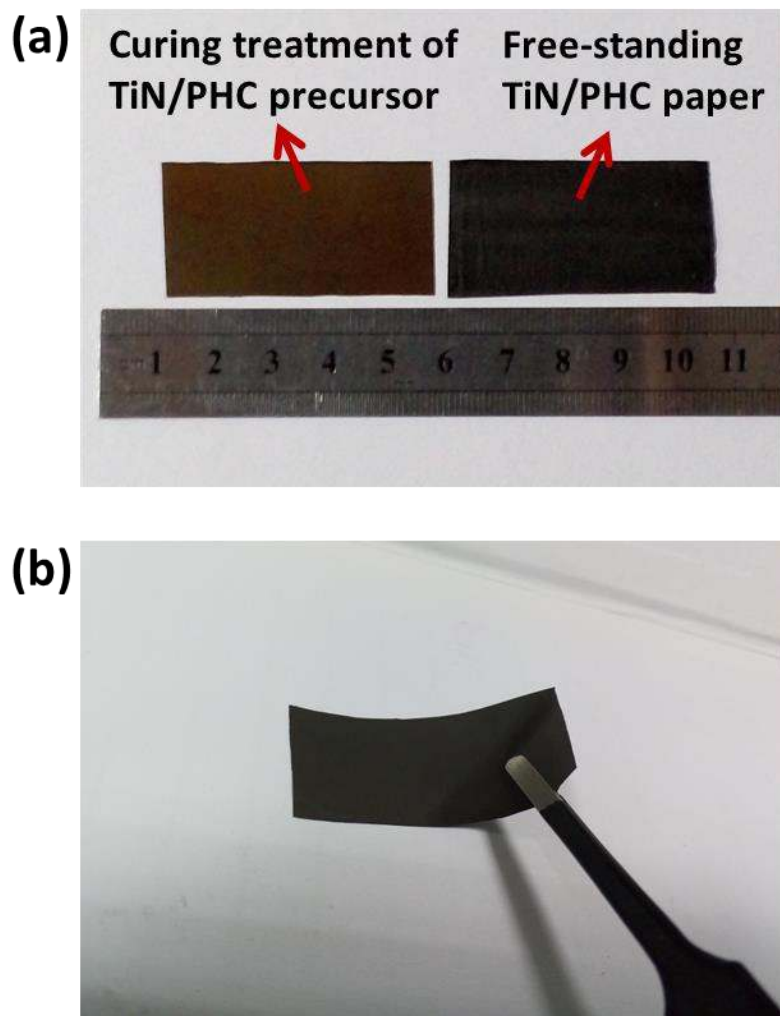
Figure S3 Photos of (a) curing treatment of TiN/PHC precursor and free-standing TiN/PHC

paper, (b) flexible free-standing TiN/PHC paper.
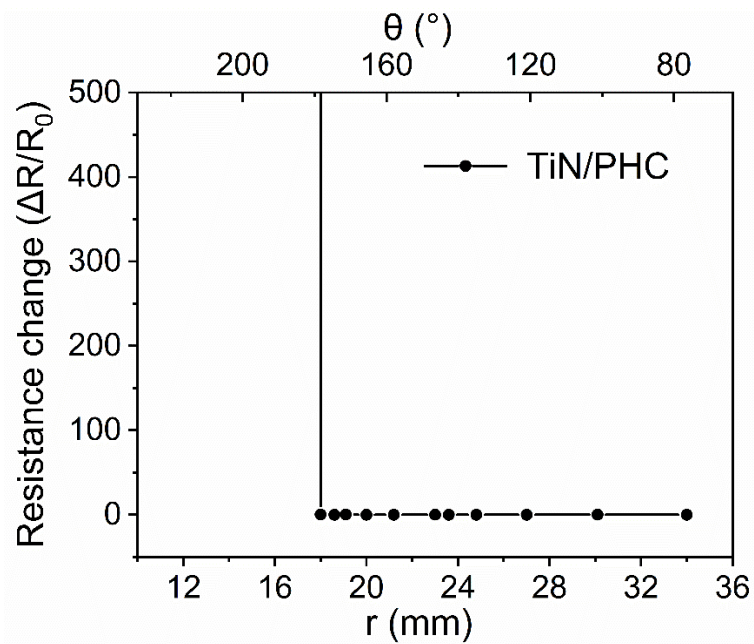
Figure S4 Relative change of resistances of TiN/PHC paper as a function of bending radius (r) and bending angle (θ).
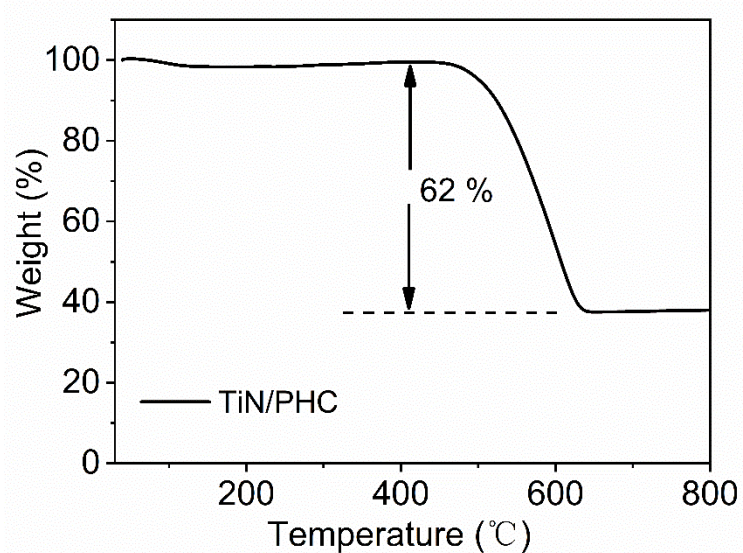
Figure S5 TG curve of the TiN/PHC host in oxygen atmosphere with a heating rate of 10 °C min^{-1} from 30 to 800 °C.
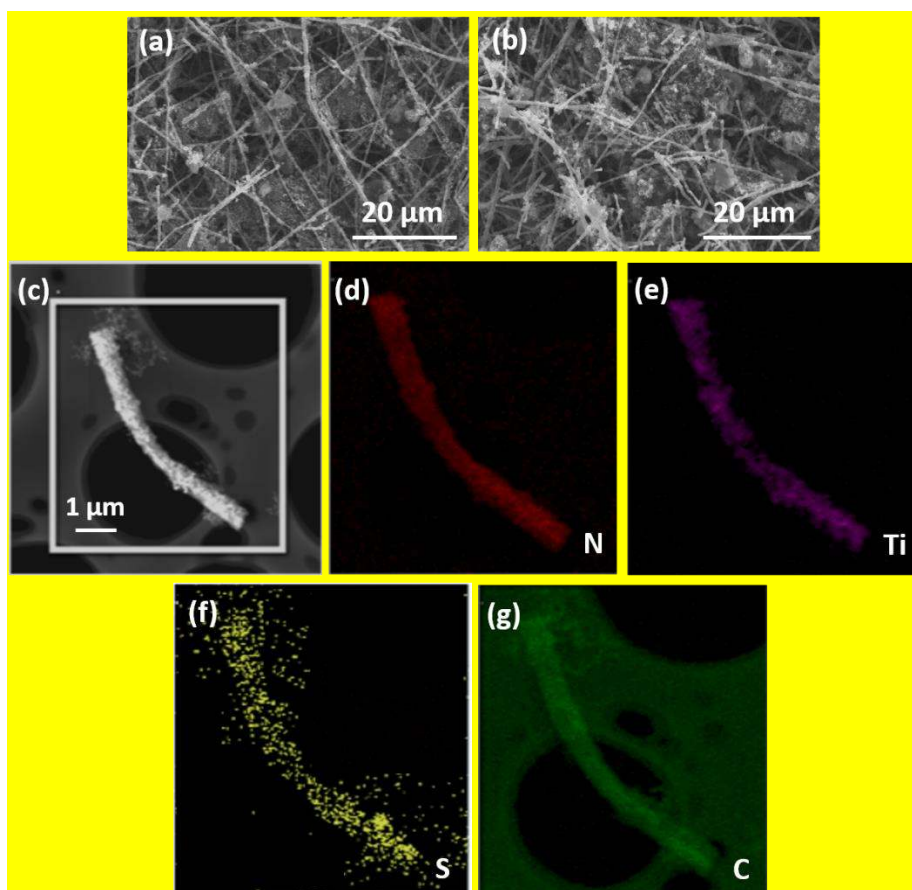
Figure S6 Characterizations of the TiN/PHC@Li$_2$S. (a, b) SEM image of TiN/PHC@Li$_2$S fibers, (c) dark-field TEM image of TiN/PHC@Li$_2$S fibers and corresponding element mappings of (d) titanium, (e) nitrogen, (f) sulfur and (g) carbon.
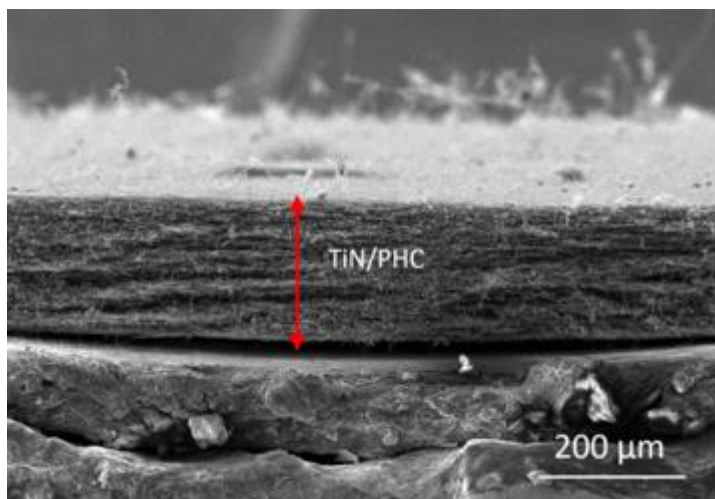
Figure S7 Cross-sectional SEM image of the TiN/PHC cathode. The thickness of the TiN/PHC is about 220 µm, and the diameter of the cathode is 8 mm. The calculated cathode volume is 11.1 mm^3.
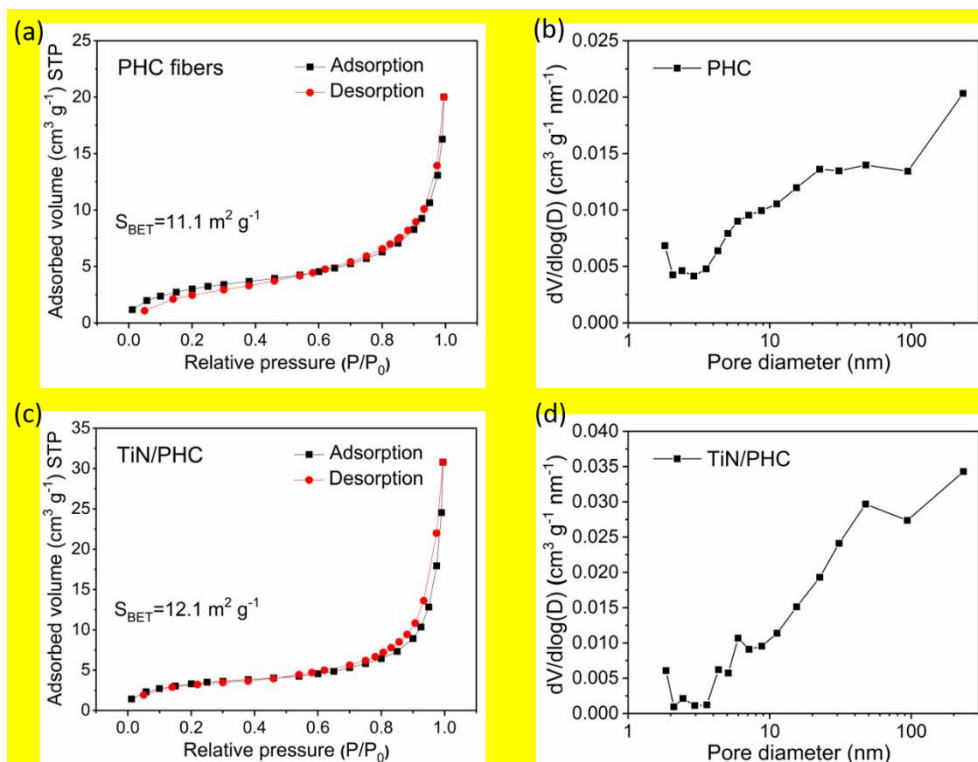
Figure S8 (a) Nitrogen sorption isotherm and (b) pore size distribution of PHC, above (c) nitrogen sorption isotherm and (d) pore size distribution of TiN/PHC.
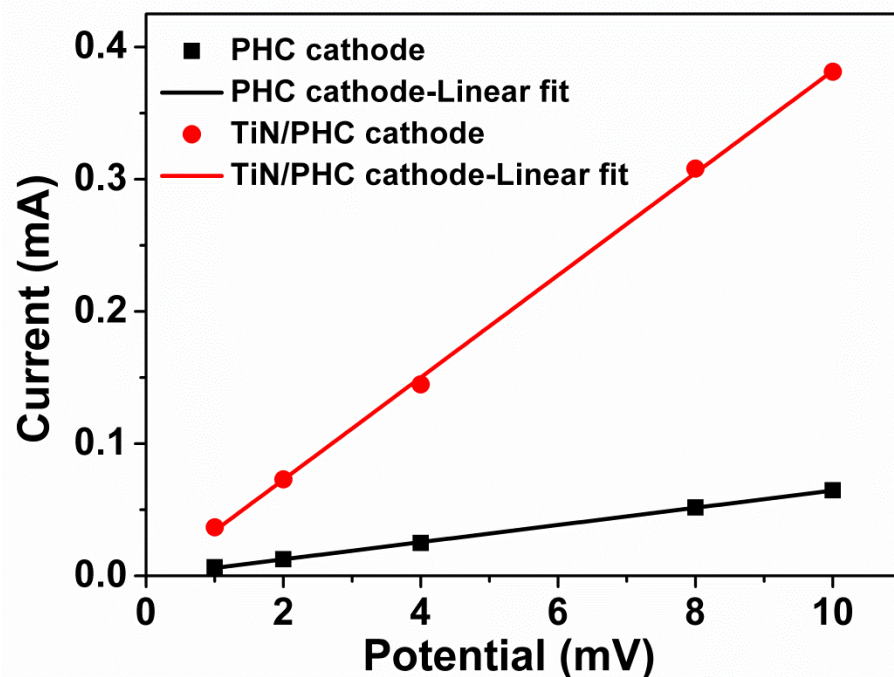
Figure S9 Current *vs.* potential profiles of PHC cathode and TiN/PHC cathode measured by Hebb-Wagner polarization method. The currents were measured at the potentials of 1, 2, 4, 8 and 10 mV, and the slope of the curves is the electronic conductivity of PHC (0.07 mS cm^{-1}) and TiN/PHC cathode (0.39 mS cm^{-1}).
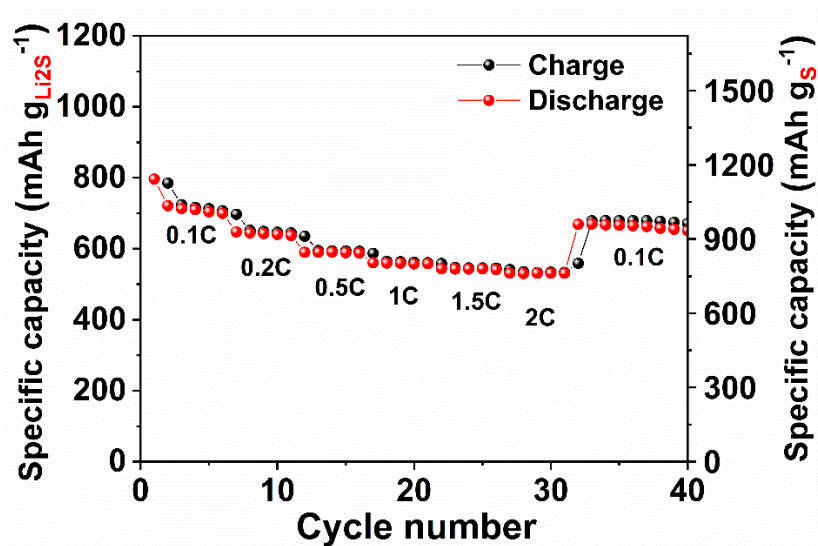
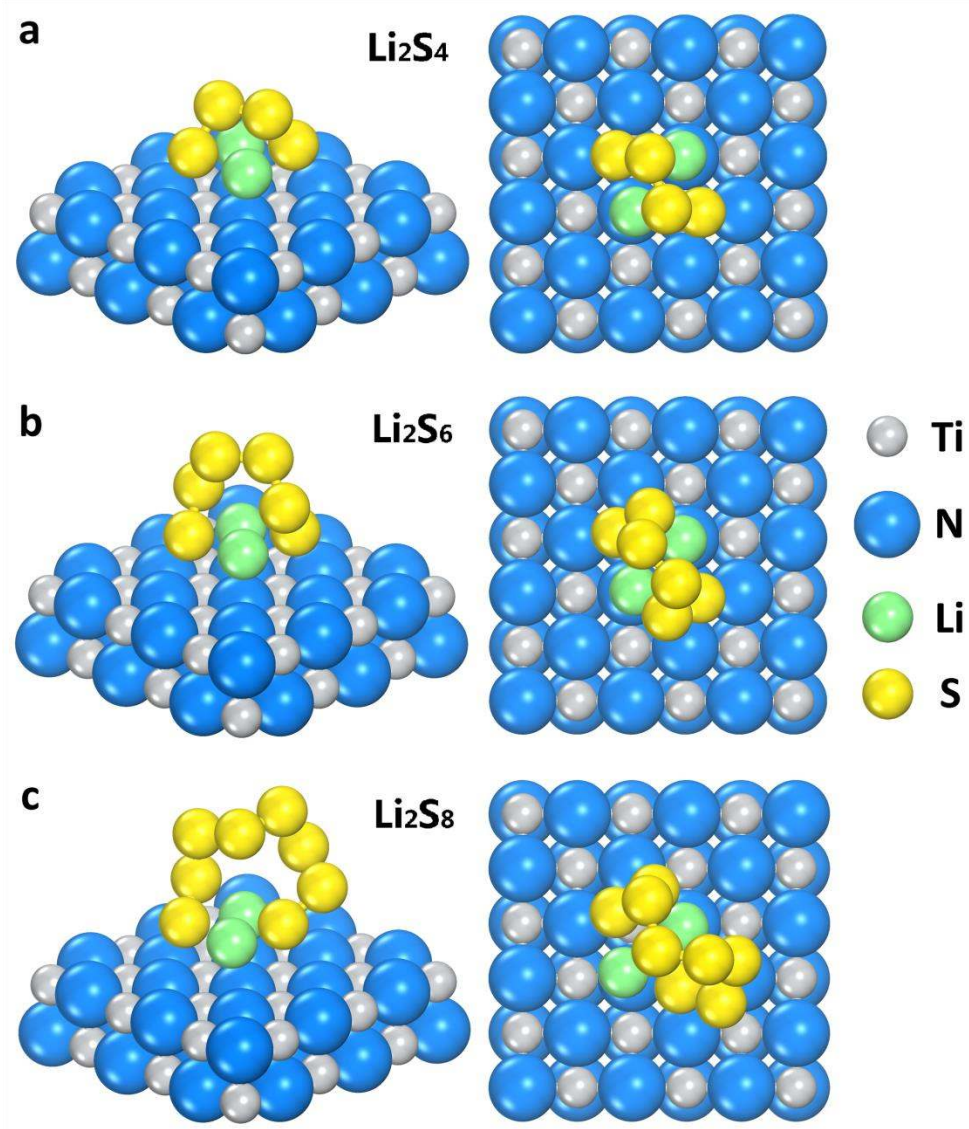**Figure S10** Rate performance of the PHC@Li$_2$S cathode *vs.* Li for half-cell with a current rate ranging from 0.1 to 2 C rate.

Figure S11 The adsorption structures of (a) Li_2S_4, (b) Li_2S_6 and (c) Li_2S_8 on TiN (200). Color

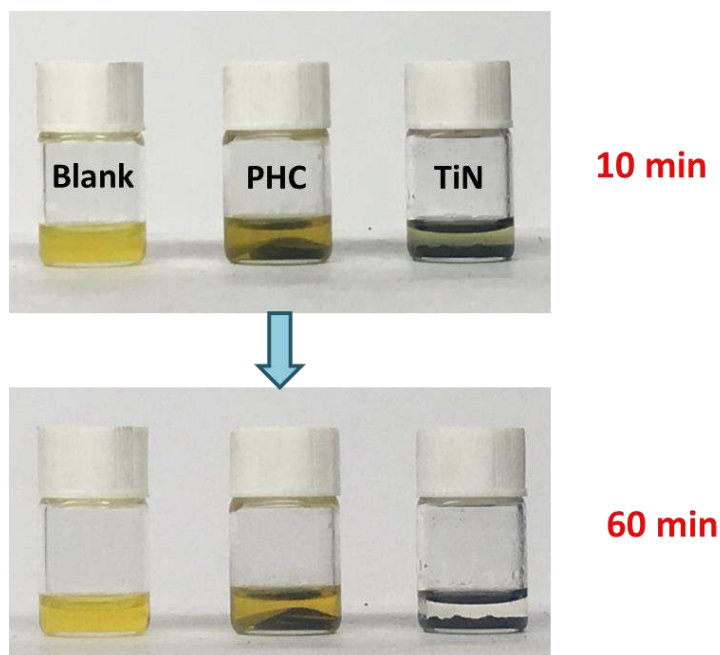scheme: gray, Ti; blue, N; green, Li; yellow, S.

Figure S12 Visual absorbent experiment. Li_2S_6 solution (0.4 mg ml^{-1}) with PHC and TiN: (a)
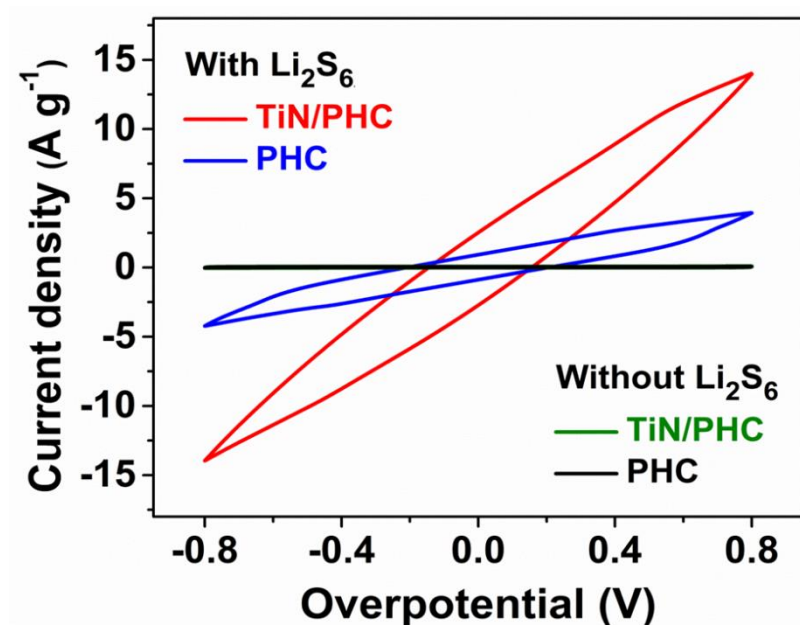
after 10 min, and (b) after 60 min.

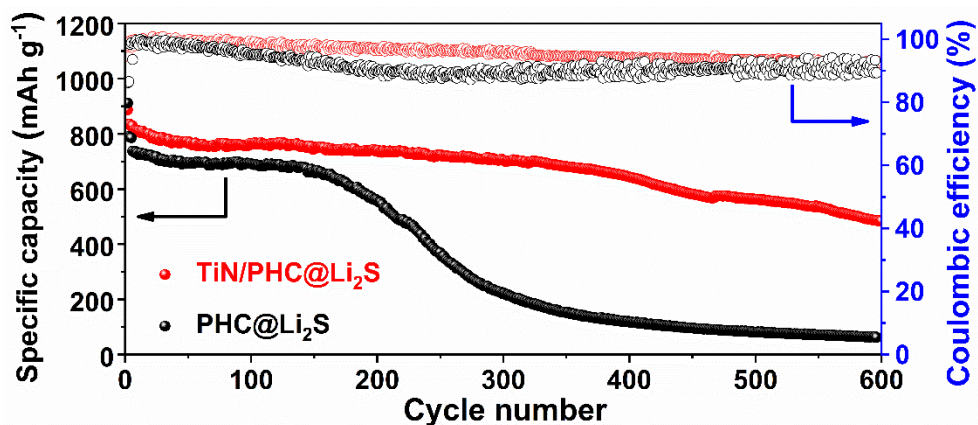**Figure S13** Polarization curves of dynamically enhanced polysulfide redox by TiN/PHC and

PHC host.

Figure S14 Cycling performance and Coulombic efficiency of TiN/PHC@Li$_2$S and PHC@Li$_2$S cathode *vs.* Li half cell at 1 C rate.
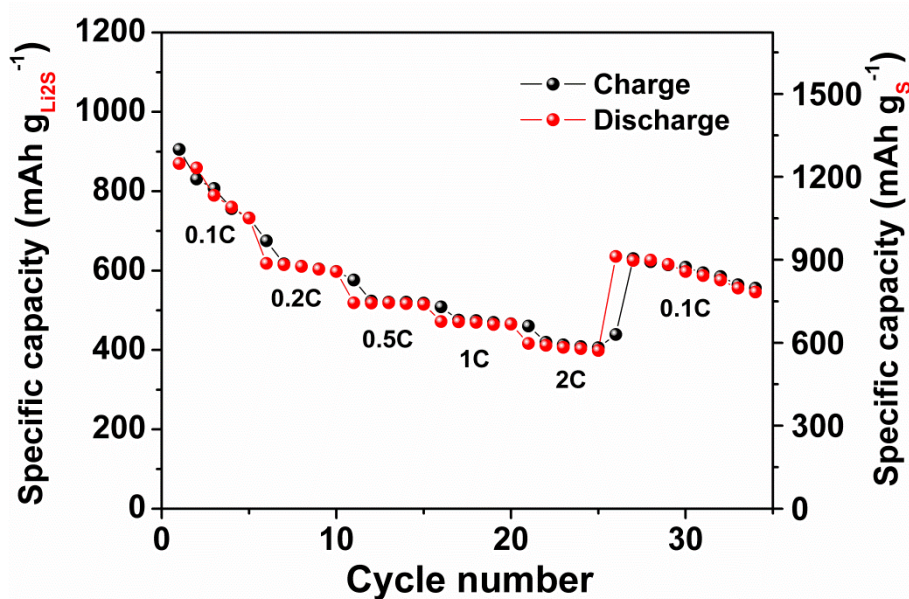

Figure S15 Rate performance of the TiN/PHC@Li$_2$S cathode *vs.* Si for full cell with a current rate ranging from 0.1 to 2 C rate.
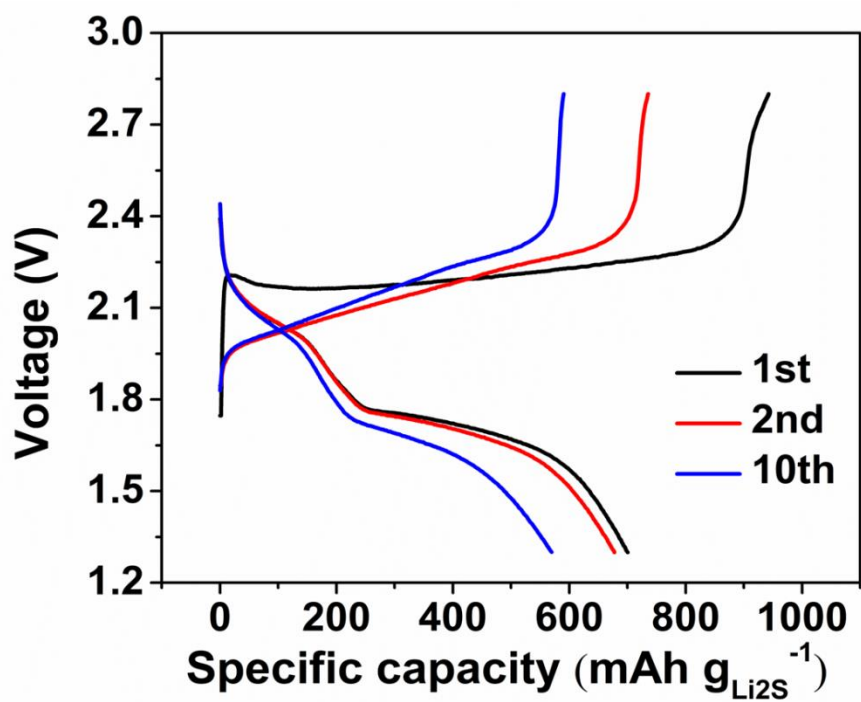
Figure S16 Voltage *vs.* specific capacity profiles at 0.5 C during cycling for TiN/PHC@Li$_2$S
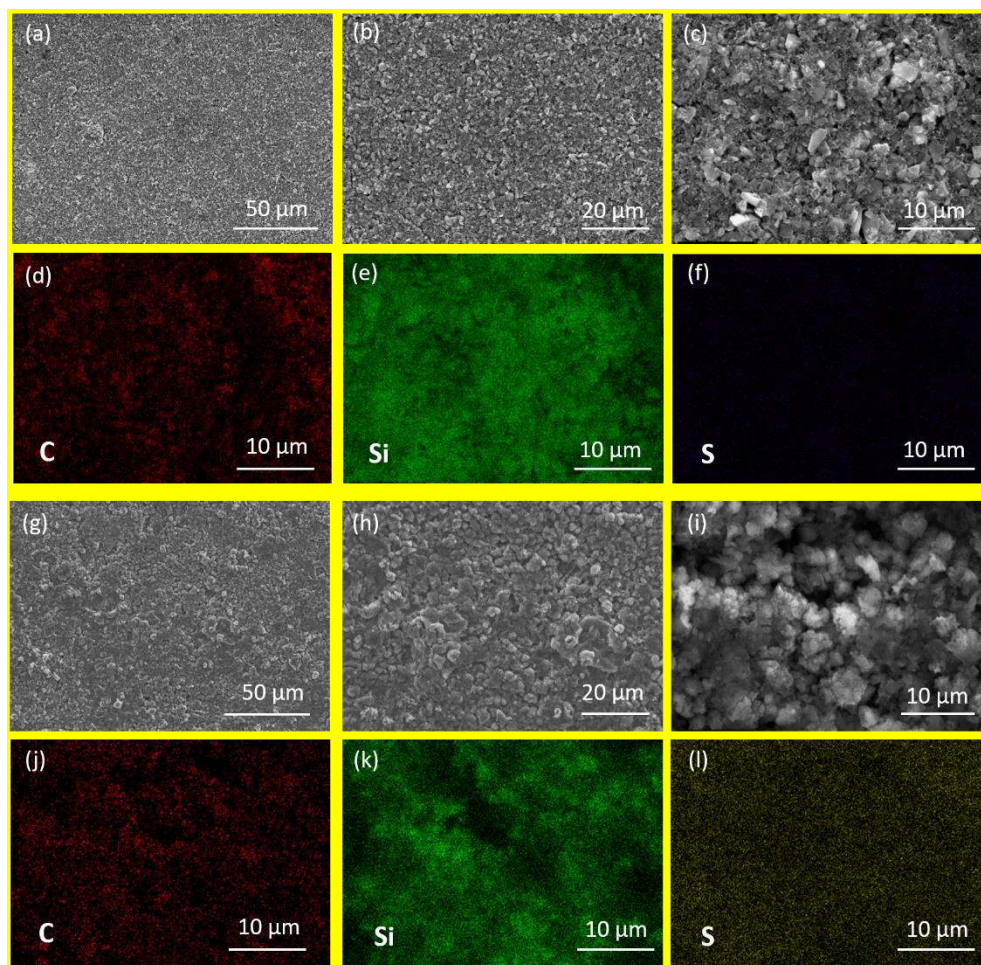
vs. Si full cell.

Figure S17 SEM image of (a-c) Si electrode before cycle and corresponding element mapping of (d) carbon, (e) Silicon, and (f) sulfur at the same region of image (c). SEM image of (g-i) Si electrode after 50 cycles at 0.5 C, and corresponding element mapping of (j) carbon, (k) Silicon, and (l) sulfur at the same region of image (i).

Table S1. Adsorption energies and bond lengths of Li_2S_4, Li_2S_6 and Li_2S_8 on TiN (200).

Adsorbate	Ti-S Bond (Å)	N-S Bond (Å)	E_{ads} (eV)
Li_2S_4	2.71	2.89	- 4.41
Li_2S_6	2.65	2.85	- 4.35
Li_2S_8	2.64	2.83	- 4.40

Table S2. Data for estimation of the Li$_2$S cell energy density

Design parameters for Calculations of Cell Energy Density	
Cell part	Weight of Material for cell (mg cm^{-2})
Cu foil	4.5
Si electrode(including binder/additives)	2
Electrolyte and separator	5
Li$_2$S electrode (including binder/additives)	4.8
Current collector (TiN/PHC)	2.8
Total	19.1

The table of contents entry

An advanced Li₂S/Si full-cell is constructed with TiN modified parallel hollow carbon (PHC) as hybrid host for Li₂S cathode, in which Li₂S is loaded by simple slurry-coating method. The present work can provide new view for the material scientists to discover high-efficiency and flexible free-standing Li₂S cathode and hence design high-performance full-cell.

Keywords: Li₂S/Si full battery, TiN polysulfide immobilizer, DFT calculations, lithium-sulfur battery

Zhangxiang Hao,‡ᵃ Jie Chen,‡ᵃ Lixia Yuan,*ᵃ Qiming Bing,ᵇ Jingyao Liu,ᵇ Weilun Chen,ᵃ Zhen Li,ᵃ Feng Ryan Wang,ᶜ Yunhui Huang*ᵃ

Advanced Li₂S/Si full battery enabled by TiN polysulfide immobilizer